Journal of Materials Chemistry A

ROYAL SOCIETY OF CHEMISTRY

PAPER

View Article Online
View Journal | View Issue

Check for updates

Cite this: J. Mater. Chem. A, 2024, 12, 6341

Four-arm star-shaped high-performance poly(aryl piperidine) anion exchange membranes for fuel cells†

Long Han,[ab] Shoutao Gong,[ab] Xinli Zhang,[ab] Min Yang,[ab] Xiaoming Yan,[ab] Gaohong He[ab] and Fengxiang Zhang *[ab]

Received 5th January 2024
Accepted 6th February 2024

DOI: 10.1039/d4ta00092g

rsc.li/materials-a

Anion exchange membrane fuel cells (AEMFCs) are a new generation of energy conversion technology that excels proton exchange membrane fuel cells in terms of oxygen reduction kinetics. The development of high-performance and durable anion exchange membranes (AEMs) has been a top priority for AEMFCs. In this work, we design and fabricate a novel series of AEMs by co-polymerizing tetraphenylmethane with 1-methyl-4-piperidone and *p*-terphenyl and subsequent quaternization of the resulting polymer. This strategy creates four-arm star shaped polymer components in the fabricated AEMs so that the polymer chain packing density is lowered, creating a high fraction of free volume in the membrane, which can help build ion channels with lower OH^- transport resistance. The resulting qPTTP-7 AEM shows a markedly improved ion conductivity (142.71 mS cm^{-1} at 80 °C). After 1000, 2000 and 3000 h treatments in 1 M NaOH at 80 °C, the membrane showed an ion conductivity retention rate of 98%, 93% and 86%, respectively. With such an AEM, the H_2–O_2 single cell yields a peak power density of 1.37 W cm^{-2} at 80 °C, and the fuel cell can operate at a constant current over 150 h without much voltage decay.

1 Introduction

Fuel cells exhibit an innate capability to transform chemical energy into electrical energy with notable efficiency, and crucially, without incurring substantial environmental pollution.[1–3] Within the domain of fuel cell technologies, proton exchange membrane fuel cells (PEMFCs) are advantageous in terms of power density and cell durability due to the utilization of high-performance Nafion membranes.[4–6] Nevertheless, PEMFC advancement has not been devoid of challenges, particularly owing to the pervasive reliance on expensive platinum group metals (PGMs) as the eletrocatalysts.[5,7–10] In this context, anion exchange membrane fuel cells (AEMFCs) have attracted considerable attention as a promising alternative to their PEMFC counterparts. The rationale behind this burgeoning interest is rooted in the superior oxygen reduction kinetics and the cost-effectiveness of catalysts attributed to the high-pH working conditions within AEMFCs, which collectively position them as viable substitutes for PEMFCs.[11–14]

At present, the main challenge obstructing the practical development of AEMFCs is to design AEMs with excellent ion conductivity and high alkali stability.[15–17] One pivotal avenue towards enhancing ion conductivity resides in the augmentation of ion exchange capacity (IEC). However, such improvements in IEC often lead to higher water uptake (WU) and swelling ratio (SR), which may damage the mechanical stability of AEMs. For instance, the PBP-6-Pip membranes synthesized by Liu *et al.* had an IEC of 3.97 mmol g^{-1}, and their WU and SR reached 189.6% and 69.5%, respectively, at an elevated temperature of 80 °C; therefore, compared with PBP-8-Pip membranes (3.76 mmol g^{-1}) with WU and SR of 162.9% and 60.9%, its tensile strength decreased from 53.23 MPa to 42.32 MPa.[18] In terms of alkali stability, AEMs prepared from polymers such as polysulfone,[19] poly(aryl ether ketone),[4,20] and poly(phenyl oxide)[21,22] contain aryl ether bonds and are prone to attack by OH^-, thereby exacerbating the degradation of AEMs.[9,23] Previous studies have shown that using aryl-ether free polymers and piperidinium-type cationic groups can effectively improve the performance of AEMs.[8,24] Bae *et al.* demonstrated the synthesis of high molecular weight poly(biphenyl olefin) membranes with exceptional resistance to alkaline conditions.[25] Hu *et al.* prepared poly(aryl piperidine) membranes, which showed no degradation even after prolonged immersion in 1 M KOH for 2000 hours.[26]

In order to better improve the performance of AEMs, one of the typical strategies is to induce microphase separation and construct efficient ion channels, thereby achieving high conductivity.[27] However, microphase separation still depends largely on IEC.[12] AEMs containing large volume and rigid

[a]State Key Laboratory of Fine Chemicals, Dalian University of Technology, Dalian 116024, China. E-mail: zhangfx@dlut.edu.cn

[b]School of Chemical Engineering, Ocean and Life Sciences, Dalian University of Technology, Panjin 124221, China

† Electronic supplementary information (ESI) available. See DOI: https://doi.org/10.1039/d4ta00092g

structural units can achieve high ionic conductivity at relatively low IEC because such units can decrease chain packing density, thereby increasing the free volume within the membrane and reducing the transport resistance of OH^-.[11,28] For instance, Gao *et al.* compared an ordinary linear tetraphenyl piperidine membrane (QAQPP) with an aryl piperidine membrane containing bis(naphthyl) (QABNP); at 80 °C, the highest OH^- conductivity of the QABNP membrane could reach 135.25 mS cm^{-1}, while the conductivity of the QAQPP membrane was only 109.12 mS cm^{-1}.[1]

Based upon the above considerations, we herein report a simple synthetic route to fabricate a novel series of AEMs by co-polymerizing tetraphenylmethane (TPM) with *p*-terphenyl and 1-methyl-4-piperidone and subsequent quaternization, which gives a copolymer qPTTP. The use of TPM in the synthesis produces four-arm star shaped polymer components, which would decrease chain packing density in the resulting AEMs, creating a high fraction of free volume and thus building ion channels with lower OH^- transport resistance. The conductivity of the resulting qPTTP-7 (7 denotes the percentage of TPM in the monomer mixture for polymerization) AEM reaches 142.71 mS cm^{-1} at 80 °C. After 3000 h treatment in 1 M NaOH at 80 °C, the membrane shows an ion conductivity retention rate of 86.45%. Employing qPTTP-7 AEM, the H_2–O_2 single cell yields a peak power density of 1.37 W cm^{-2} at 80 °C, and the fuel cell can operate at a constant current over 150 h without much voltage decay.

2 Experimental

2.1. Materials

p-Terphenyl (98%), dimethyl sulfoxide (DMSO), tetraphenylmethane (TPM, 97%), 1-methyl-4-piperidone (mPip, 98%), trifluoromethanesulfonic acid (TFSA, 99%) trifluoroacetic acid (TFA, 99%), dichloromethane, sodium hydroxide (NaOH), iodomethane, and potassium carbonate were used as received.

2.2. Synthesis of polymers

2.2.1. Copolymerization of TPM, *p*-terphenyl and mPip to give PTTP-*x*. PTTP-*x* (*x* is the molar percentage of TPM in the monomers) was synthesized using a super acid catalytic method. Taking the synthesis of PTTP-5 as an example, TPM (0.08 g, 0.25 mmol), *p*-terphenyl (1.09 g, 4.75 mmol), and mPip (0.70 mL, 6 mmol) were dissolved in 2.50 mL dichloromethane; trifluoroacetic acid (TFA, 0.40 mL, 5.4 mmol) and trifluoromethanesulfonic acid (TFSA, 6.00 mL, 75 mmol) were incrementally introduced into the above solution. This controlled addition of reagents was executed while maintaining a low temperature of 0 °C. The reaction, under precisely controlled conditions, was allowed to proceed in 6 hours, yielding a black, highly viscous solution. The resulting mixture was precipitated in 1 M NaOH solution to obtain light yellow fibers, which were then filtered, and washed with deionized water until neutral, and dried at 80 °C to give the final product. Incorporation of higher amount of TPM, for example 9%, led to excessive cross-linking and gelation in the polymer, which cannot be used for membrane fabrication.

2.2.2. Quaternization of PTTP-*x* to give qPTTP-*x*. Taking qPTTP-5 as an example, the procedure commenced with the dissolution of PTTP-5 (1.23 g) in 25 mL DMSO, to which an excess of iodomethane (0.75 mL, 12 mmol) and potassium carbonate (1.47 g, 10 mmol) were introduced. The reaction proceeded at 40 °C for 48 h. After the reaction was completed, the mixed solution was precipitated in ethyl acetate; the product was washed several times with ethyl acetate and deionized water to remove the excess material, and finally dried at 80 °C to obtain a light white solid. Fig. 1a illustrates the entire synthesis process. For comparison purposes, qPTTP-0 (without TPM units) was also synthesized (Fig. S1†).

2.3. Membrane preparation

For membrane fabrication, a 5 wt% DMSO solution of qPTTP-*x* was filtered using an organic filter membrane with a pore size of 0.8 μm. The filtered solution was cast on a glass plate and heated at 60 °C for 24 h. The obtained AEMs were immersed in 1 M NaOH for 48 h to complete the alkali exchange. Fig. 1b shows the 24 × 24 cm^2 membrane obtained and casting solution of qPTTP-*x*; the membrane can be stretched and folded freely without any breakage, indicating its good toughness. The thickness of the membranes involved in characterization was around 23 μm.

2.4. Characterization

2.4.1. Chemical structure and morphology. The chemical structures of membrane materials were determined using ^{1}H NMR on a Bruker 500AVANCEII spectrometer (500 MHz) with dimethyl sulfoxide-d_6 as a solvent. A JEOL JEM-2000EX transmission electron microscope was used to acquire the transmission electron microscopy (TEM) image of the membrane. Samples were processed as follows before the TEM test: 10 μL of the 5 wt% membrane solution was dropped onto copper mesh. The sample was dried at 60 °C for 24 h, then soaked in 1 M potassium iodide solution for 24 h, and washed with DI H_2O to remove KI. Finally, the sample was dried at 80 °C to constant weight. The small-angle X-ray scattering (SAXS) spectra of dry membranes were obtained using a D8 Advance X-ray diffraction system with scattering angles of 0.5–5°.

The fractional free volume (FFV) was calculated from eqn (1). The specific apparent volume (V) was calculated from eqn (2). In these equations, L_1, L_2, and L_3 are the length, width, and thickness of the membrane, respectively, each being the average of multiple measurements, and m_d represents the mass of the membrane after drying. The specific skeleton volume (V_0) was determined from eqn (3), where the skeleton volume (V_d) was measured on a Micromeritics AccuPyc II 1340 instrument by a helium pycnometer method and the average value was taken from five measurements.

$$\mathrm{FFV} = \frac{V - V_0}{V} \quad (1)$$

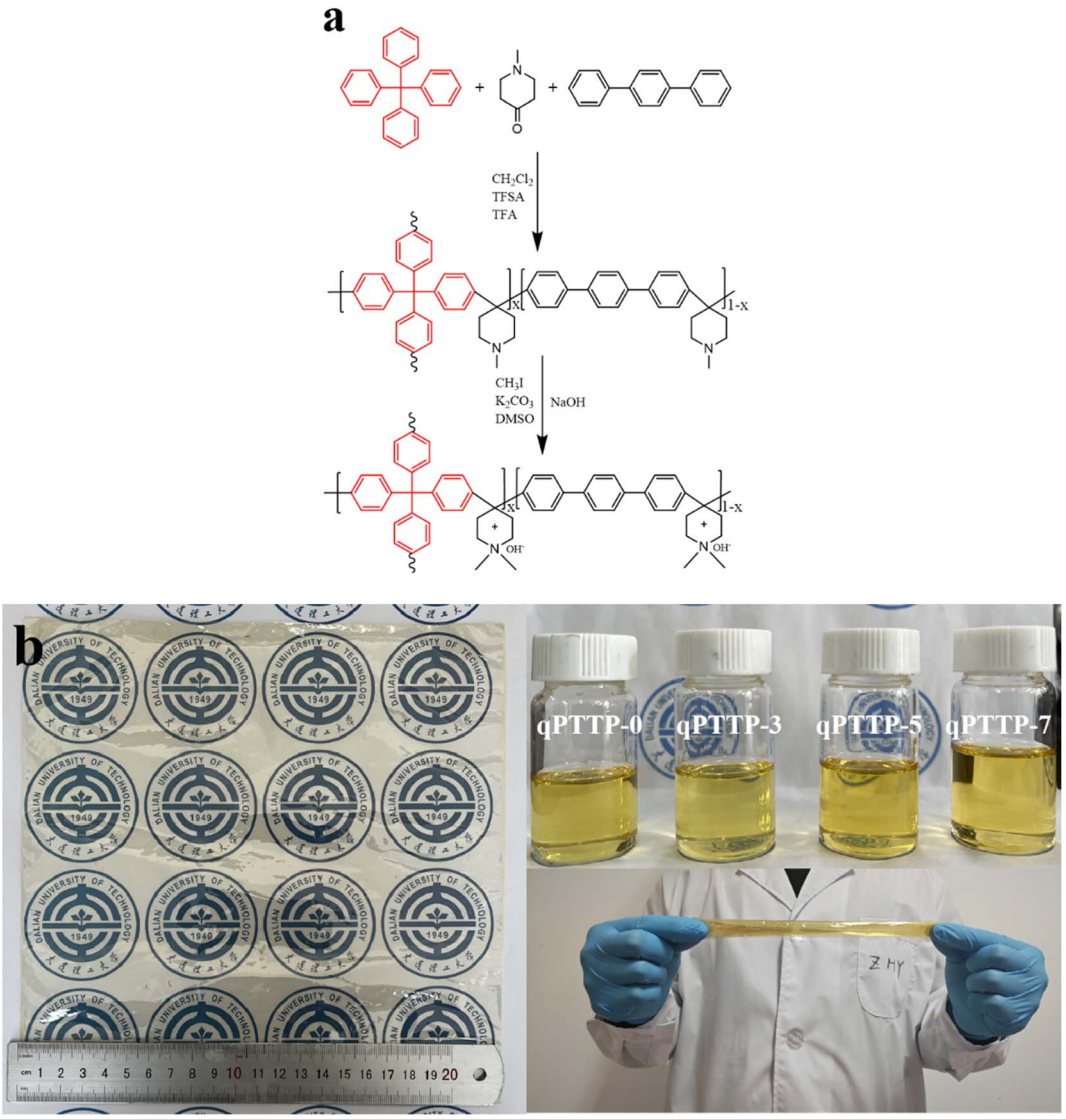

Fig. 1 (a) Synthesis route of qPTTP-*x*; (b) photos of the casting solution, 24 × 24 cm^2 qPTTP-7 membrane and the membrane stretched and folded.

$$V = \frac{L_1 L_2 L_3}{m_d} \quad (2)$$

$$V_0 = \frac{V d V_d}{m_d} \quad (3)$$

2.4.2. Thermal, mechanical, and chemical stability. Thermogravimetric analysis (TGA) was conducted in a nitrogen atmosphere within the temperature range of 30–800 °C, employing a ramping rate of 10 °C min^{-1}. Prior to the examination, the membranes were subjected to drying until a constant weight was achieved. Tensile strength and elongation at break were assessed using a SANS analyzer. The chemical stability was explored by immersing the membrane in 1 M NaOH solution at 80 °C, extracting it at various time intervals, rinsing with deionized water, and subsequently evaluating the conductivity retention and chemical structure alterations using ^{1}H NMR.

2.4.3. Ion exchange capacity (IEC). The Mohr titration was used to characterize the IEC of the membrane. A sample (in Cl^- form) was soaked in a 0.5 M sodium sulfate solution for 48 h and then titrated with a 0.01 M $AgNO_3$ solution using potassium chromate solution as an indicator. IEC could be calculated using eqn (4).

$$\mathrm{IEC} = \frac{C_{\mathrm{AgNO_3}} V_{\mathrm{AgNO_3}}}{W_{\mathrm{dry}}} \quad (4)$$

2.4.4. Water uptake (WU) and swelling ratio (SR). The membrane samples with a regular shape were kept in water for 12 h at different temperatures, and the moisture on the membrane surface was removed quickly. The dimension and weight of the wet membranes were measured at this

temperature. Then the membranes were dried under vacuum at 50 °C for 24 h, and the dimension and weight were measured again. WU and SR were calculated from eqn (5) and (6), respectively, where W and L represent the weight and dimension of samples, respectively. $L_{wet} = (L_{wet1} \times L_{wet2})^{1/2}$, and $L_{dry} = (L_{dry1} \times L_{dry2})^{1/2}$. The length and width of the sample in the dry state and the wet state are, respectively, denoted as L_{dry1}, L_{dry2}, L_{wet1}, and L_{wet2}.

$$WU = \frac{W_{wet} - W_{dry}}{W_{dry}} \quad (5)$$

$$SR = \frac{L_{wet} - L_{dry}}{L_{dry}} \quad (6)$$

2.4.5. Ion conductivity. Ion conductivity was measured by a four probe-electrode AC impedance method in constant current mode in the range of 1–10^5 Hz. The outcome is presented in eqn (7), wherein L represents the spacing between two proximate electrodes, A denotes the cross-sectional area of the specimen, and R corresponds to the ohmic resistance of the membrane derived from electrochemical impedance spectroscopy (EIS).

$$\sigma = \frac{L}{RA} \quad (7)$$

2.4.6. Alkaline stability. The AEM was submerged in 1 M NaOH solutions (periodically renewed) at 80 °C for varying durations; the ion conductivity of the processed AEMs was measured at 25 °C. ^{1}H NMR spectra of the AEM following alkaline treatment were captured to detect chemical changes in the membrane.

2.5. Fuel cell performance

Poly(diphenyl piperidinium) (PBP) was synthesized and used as the catalyst binder; its synthesis and performance are shown in Fig. S2 and S3,† respectively. For catalyst ink preparation, a specific quantity of Pt/C (40 wt% Pt, for the cathode) or Pt–Ru/C (40 wt% Pt, 20 wt% Ru, for the anode), and PBP (5 wt% DMSO solution) were dispersed in a mixed solvent of water/isopropyl alcohol (1 : 9), and subjected to ultrasonication for 30 min. The resulting anode- and cathode catalyst inks were then sprayed onto the two sides of a dry membrane, respectively, to prepare the catalyst coated membrane (CCM). The catalyst metal loading on each side remained at 0.4 mg cm^{-2}, and the effective area amounted to 4 cm^2. Preceding the test, the CCM underwent immersion in 1 M NaOH for 24 h, followed by three rinses with DI water. The CCM was then interposed between two gas diffusion layers to fabricate a membrane electrode assembly (MEA), which was then assembled with two end plates to construct a fuel cell device (Scheme 1). Hydrogen and oxygen gases were introduced to the MEA *via* the two end plates at a flow rate of 1000 cm^3 min^{-1}, maintaining a relative humidity of 100%. The fuel cell durability test was implemented at a constant current density of 200 mA cm^{-2} at 60 °C, and the temporal changes in voltage were systematically recorded.

3 Results and discussion

3.1. Synthesis and characterization

Chemical structures of the synthesized polymers were analyzed through ^{1}H NMR spectroscopy. Fig. 2a shows the spectrum of PTTP-0, where the signals for the benzene ring (7.0–8.0 ppm) and piperidine (2.1–3.8 ppm) are clearly seen. Fig. 2b displays the signals corresponding to the methylene proton of the TPM unit around 7.0–7.5 ppm (1,2), which confirms successful incorporation of the 4-arm branching unit into the ether-free main chain, and the signals at 3.56 ppm (5), 3.24 ppm (7), 2.95 ppm (4), and 2.34 ppm (8) in Fig. 2b correspond to the methylene groups of the piperidine ring and 2.86 ppm (6) corresponds to the methyl groups on N. ^{1}H NMR spectra for the two quaternized membranes, qPTTP-0 and qPTTP-7, are shown in Fig. 2c and d, respectively, where the signals at 3.35 ppm (5) and 2.92 ppm (4) correspond to the methylene proton in the piperidinium group and the signal at 3.16 ppm (6) is ascribed to the methyl groups on N. It is noteworthy that the shift in the signal of the piperidine proton following quaternization is attributed to the pronounced electron-withdrawing effect of the piperidinium cation. Based on the ^{1}H NMR results in Fig. 2 within the range of 2.1–3.8 ppm, it can be deduced that the synthesis of qPTTP has been successfully accomplished.

3.2. Membrane morphology

The OH^- conductivity of AEMs is related to their morphology; well-developed microphase separation is beneficial for fast ion transport.[29] The assessment of the quality of microphase separation structures is often accomplished through TEM images, which reveal the distinct hydrophobic and hydrophilic domains, visually represented by the bright and dark regions. As seen from the TEM images in Fig. 3, qPTTP-7 AEM (e–g) exhibits a notably more conspicuous microphase separation structure than qPTTP-0 (a–c). One plausible explanation resides in that the four-arm star shaped polymer components have the capacity to disrupt the stacking of chains and amplify free volume;[30,31] with higher volume, cation aggregation may experience smaller resistance. The morphological features of qPTTP-*x* AEMs were further probed by phase mode atomic force microscopy (AFM). As shown in Fig. 3d and h, the deep color region of the AFM images indicates aggregation of the hydrophilic piperidinium segments while the light color region indicates the aggregation of the hydrophobic aryl chains, and it is evident from the two AFM images that the qPTTP-7 AEM exhibits clearer hydrophobic/hydrophilic microphase separation. SAXS spectra (Fig. S4†) of the two AEMs were also recorded; they gave morphology information that is consistent with the result obtained from TEM and AFM. The microphase separation of qPTTP-7 is more significant because the introduction of TPM increases free volume in the membrane, which can facilitate cation aggregation to form the hydrophilic microphase. The enhancement in free volume resulting from the 4-arm star polymer can be assessed through the calculation of fractional free volume (FFV). As shown in Table 1, the FFV of qPTTP-7 AEM (0.176) significantly surpasses that of qPTTP-0 (0.077).

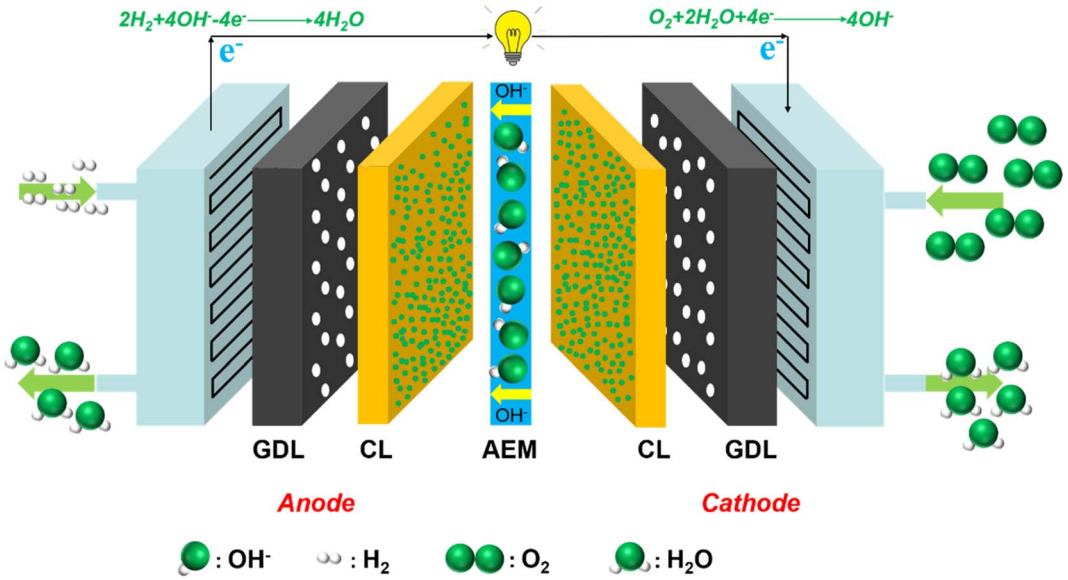

Scheme 1 Diagram of the AEMFC.

3.3 Water uptake (WU) and swelling ratio (SR)

Fig. 4a and b depict the WU and SR characteristics of qPTTP-*x* AEMs at 25–80 °C. It is evident that, as the degree of branching increases, there is a consistent and progressive augmentation in both WU and SR; specifically, the WU rises from 69.97% to 110.13%, while the SR increases from 17.49% to 29.45%, all at 25 °C. This can be mainly attributed to the gradual expansion of the free volume within AEMs, which is a direct consequence of the star shaped polymer chain. All examined AEM specimens consistently demonstrate acceptable dimensional stability when the temperature rises from 25 to 80 °C.

3.4. Ion exchange capacity and ion conductivity

It is worth reiterating that the sole elevation of IEC does not constitute a sustainable strategy for augmenting AEM conductivity. Reasonable IEC is a necessary condition to ensure high conductivity of an AEM and its structural stability. The experimental IEC of qPTTP-*x* membranes exhibits a narrow range,

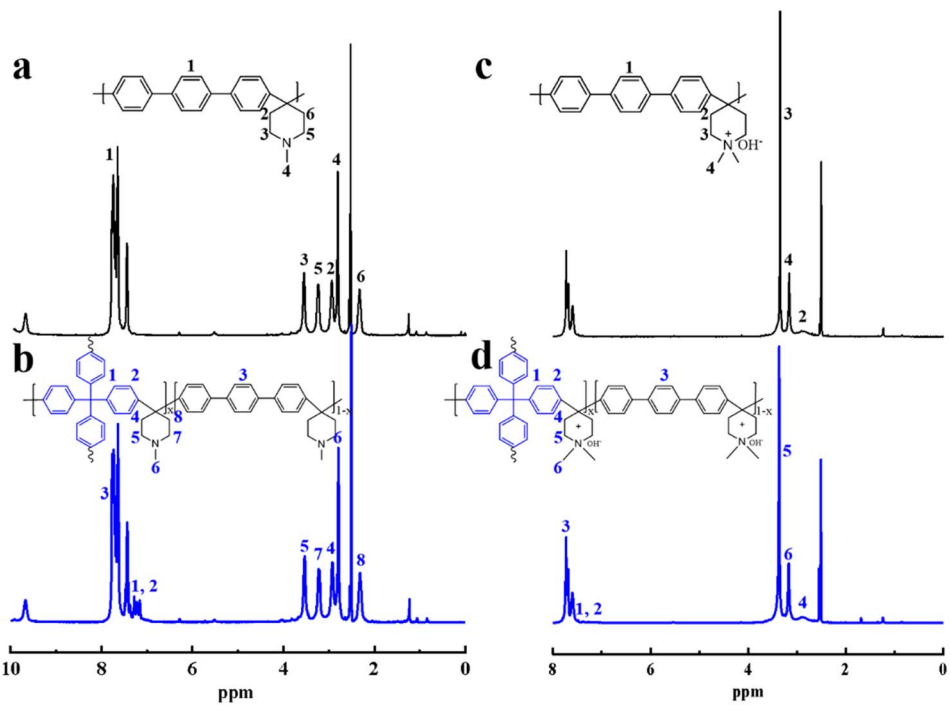

Fig. 2 The ^{1}H NMR spectra of (a) PTTP-0, (b) PTTP-7, (c) qPTTP-0 and (d) qPTTP-7.

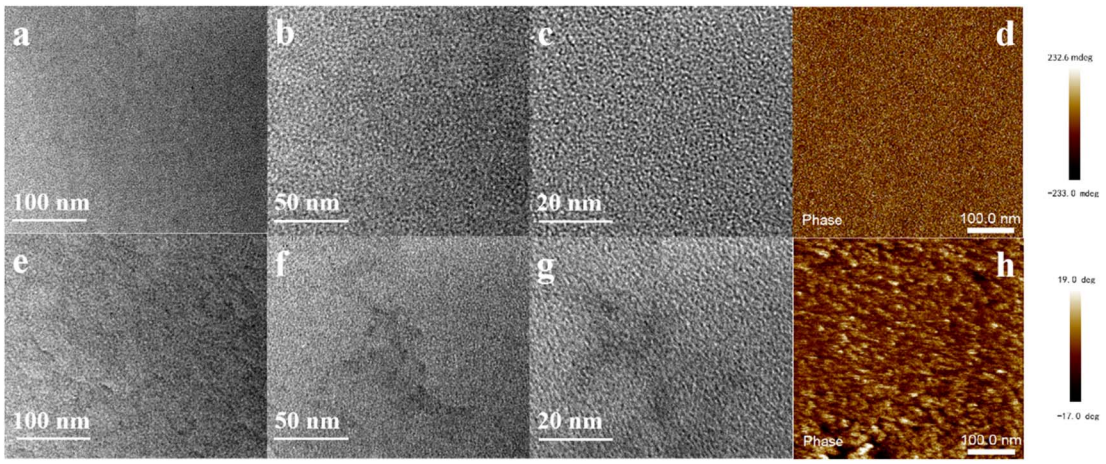

Fig. 3 TEM image of (a–c) qPTTP-0 and (e–g) qPTTP-7; phase mode AFM images of (d) qPTTP-0 and (h) qPTTP-7.

Table 1 FFV of different qPTTP AEMs

	V_0 ($cm^3\ g^{-1}$)	V ($cm^3\ g^{-1}$)	FFV ($cm^3\ cm^{-3}$)
qPTTP-0	0.707	0.766	0.077
qPTTP-7	0.705	0.857	0.176

falling within 2.75 to 2.80 mmol g^{-1}. As depicted in Fig. 5, the ion conductivity of the qPTTP-*x* AEMs increases with temperature: when the temperature is elevated from 25 °C to 80 °C, the OH^- conductivity of qPTTP-7 AEM increases from 82.86 mS cm^{-1} to 142.71 mS cm^{-1} while that of qPTTP-0 (without branching) from 54.79 mS cm^{-1} to 110.45 mS cm^{-1}. The higher conductivity of qPTTP-7 compared with that of qPTTP-0 at similar IEC values proves that the 4-arm star-shaped polymer component in the AEM is able to facilitate the formation of the well-defined microphase separation structure and establish distinct ion transport pathways.

3.5. Thermal and mechanical stabilities

As shown in Fig. S5a,† the tensile strength of qPTTP-*x* AEMs decreases with increase in the branching degree. The introduction of the branched structure restrains chain entanglement, which leads to a continuous decline in the tensile strength of AEMs and increase in the elongation at break. It is pertinent to highlight that the tensile strength of qPTTP-7 is 28.64 MPa, accompanied by an elongation at break of 13.23%. These mechanical properties are sufficient to meet the operational requirements for application in AEMFCs.

TGA curves for the two qPTTP-*x* membranes are shown in Fig. S5b.† The initial weight loss occurring at temperatures below 150 °C is attributed to the removal of residual water or any organic solvents present within AEMs. The subsequent weight loss within the temperature range of 150–400 °C is ascribed to the decomposition of piperidinium groups. The third and final degradation stages above 400 °C originate from the structural degradation of AEM backbones. It can be observed that the TGA curves of the two qPTTP membranes are similar before 400 °C, after which the qPTTP-7 membrane

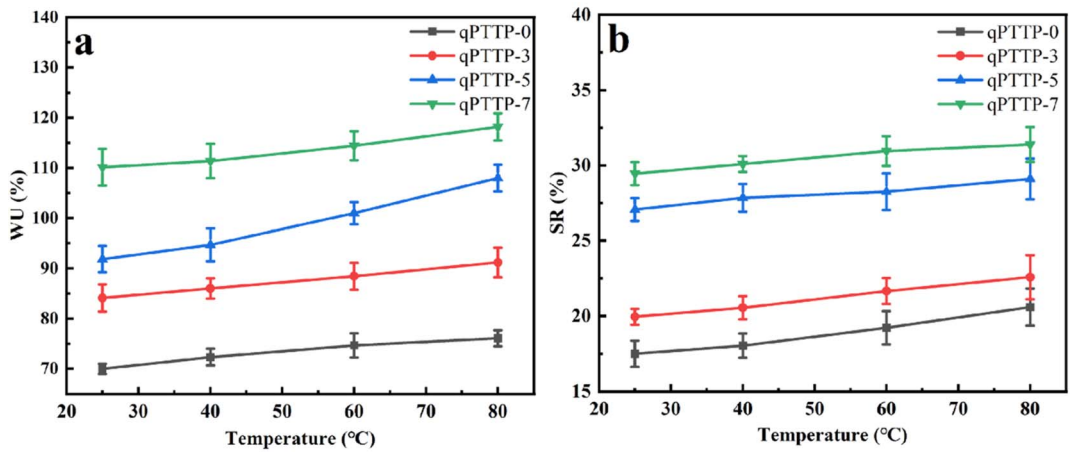

Fig. 4 WU (a) and SR (b) of qPTTP-*x* as a function of temperature.

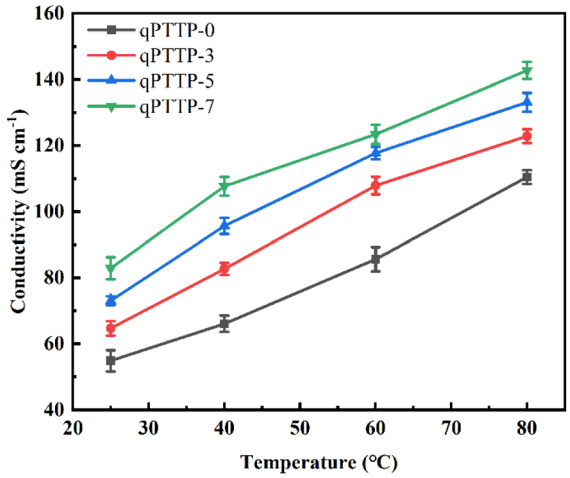

Fig. 5 Conductivity of qPTTP-*x* as a function of temperature.

shows a higher mass loss than qPTTP-0. This is consistent with their structural difference. Meanwhile, it is pertinent to note that the operational temperatures of AEMFCs typically do not exceed 100 °C, and therefore, the observed thermal stability of the qPTTP-7 membrane well meets the requisite standards for fuel cell operation.

3.6. Alkaline stability

The assessment of alkaline stability was conducted by periodic testing of conductivity changes of the membranes immersed in a 1 M NaOH solution at 80 °C. As illustrated in Fig. 6a, after an extended exposure of 1000, 2000 and 3000 h to the above alkali treatment, the qPTTP-7 AEM showed a conductivity retention of around 98%, 93% and 86%, respectively. This is a good alkali stability and can be explained as follows. Firstly, the microphase separation architecture within the qPTTP-7 enhances the solvation of OH^- and resulted in a comparatively weaker interaction between OH^- and the piperidine cationic groups. Secondly, the qPTTP-7 AEM exhibits a rigid hydrophobic framework, which serves as a protective barrier against the aggressive attack of OH^-. Thirdly, the TPM units impart a notable steric hindrance effect impeding the access of OH^- to the cationic groups, thus mitigating the degradation process.[12,32] ^{1}H NMR spectra before and after the alkali stability test are recorded and provided in Fig. 6b. The signals increase at 0.85, 1.2, and 1.5 ppm, which are attributed to the alkyl groups generated by degradation of piperidinium *via* SN_2 nucleophilic substitution. And the stability of our qPTTP-7 membrane is better than or comparable to that of recently reported AEMs as shown in Table S1.†

3.7. Fuel cell performance

The H_2–O_2 AEMFC single-cell performances of qPTTP-7 and qPTTP-0 were further evaluated. Fig. 7a shows their polarization and power density curves recorded at 80 °C without back pressure. The open-circuit voltages of AEMs are both around 1.0 V, suggesting their excellent resistance to fuel/oxidant crossover. The cell of qPTTP-7 exhibits a peak power density (PPD) of 1.15 W cm^{-2}, much higher than that of qPTTP-0 (0.65 W cm^{-2}). As illustrated in Fig. 7b, the imposition of a back pressure of 1.3 bar results in marked enhancements in the PPD of both cells, with qPTTP-7 achieving an impressive PPD value of 1.37 W cm^{-2}. This improvement is explicable by the effective utilization of catalyst active sites under high pressure conditions, in stark contrast to a scenario where only a part of the active sites is engaged in the absence of back pressure.

The durability of the H_2–O_2 fuel cell based on qPTTP-7 is shown in Fig. 7c. The cell voltage declined from 0.76 to 0.67 V at 0.2 A cm^{-2} and 60 °C in the first 5 h, while decaying slowly to 0.53 V in the following 145 h. The voltage decline may be caused by factors such as physical/chemical stability of the AEMs, the activity of the catalyst, and the water environment in the single fuel cell.[15,33,34] The voltage fluctuation during the durability test was probably due to water balancing problems caused by improper anode and cathode humidity. It is important to note that no degradation of the qPTTP-7 membrane occurred after the fuel cell operation as indicated by the ^{1}H NMR spectrum

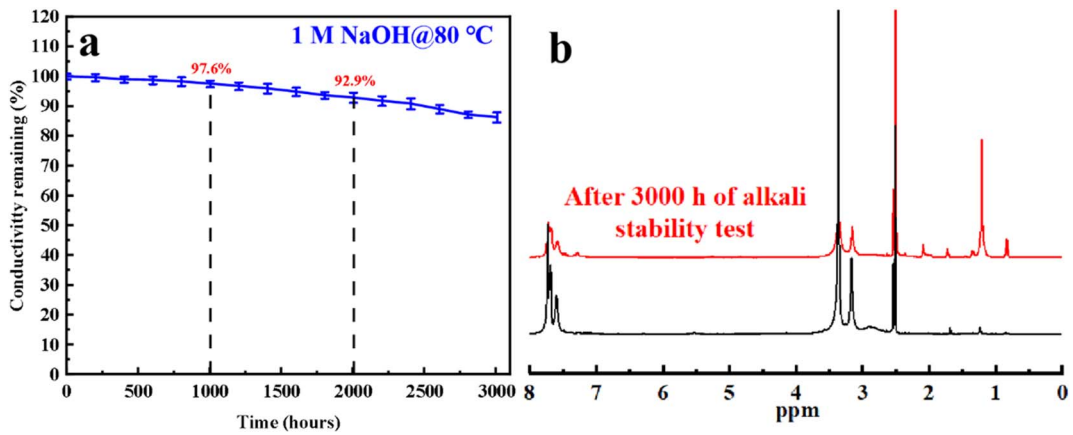

Fig. 6 (a) Conductivity retentions of qPTTP-7 in 1 M NaOH solution at 80 °C for different times; (b) ^{1}H NMR spectra of qPTTP-7 before and after the alkali stability test.

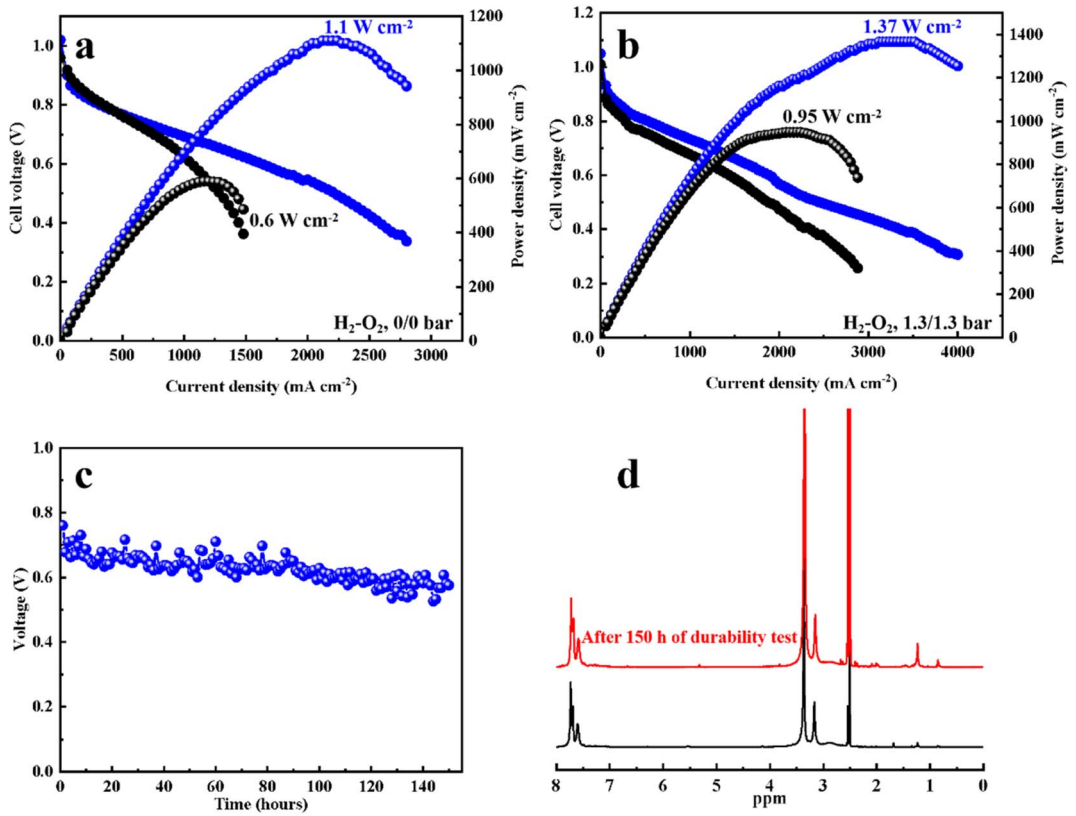

Fig. 7 (a and b) H_2/O_2 fuel cell performance of qPTTP-0 and qPTTP-7 at (a) 0/0 bar and (b) 1.3/1.3 bar back pressures, both at 80 °C, 100% RH and 1.0/1.0 L min^{-1} H_2–O_2 flow rate; (c) H_2/O_2 fuel cell durability test of qPTTP-7 under a constant current density of 0.2 A cm^{-2} at 60 °C; (d) ^1H NMR spectra of qPTTP-7 before and after the durability test.

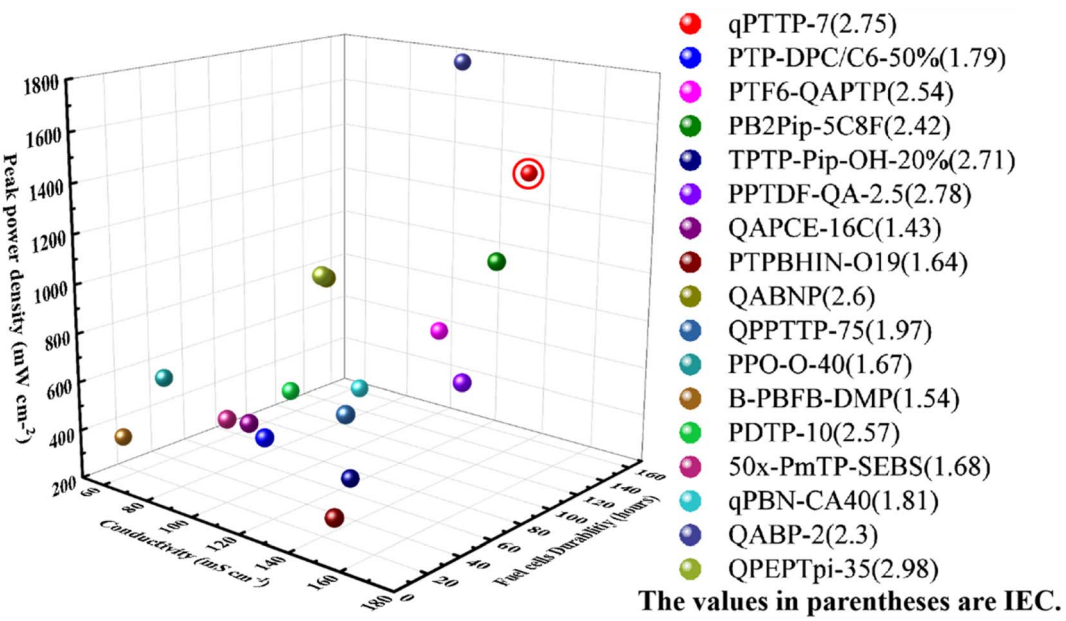

Fig. 8 Conductivity, fuel cell peak power density and durability of qPTTP-7 AEM and recently reported AEMs. References for the compared membranes: PTP-DPC/C6-50%,[10] PTF6-QAPTP,[35] PB2Pip-5C8F,[27] TPTP-Pip-OH-20%,[36] PPTDF-QA-2.5,[11] QAPCE-16C,[5] PTPBHIN-O_{19},[37] QABNP,[1] QPPTTP-75,[38] PPO-O-40,[3] B-PBFB-DMP,[39] PDTP-10,[40] 50*x*-PmTP-SEBS,[41] qPBN-CA40,[42] QABP-2,[43] QPEPTpi-35.[44]

shown in Fig. 7d. This means the voltage decline may originate from non-membrane factors. All these results indicate that the qPTTP-7 membrane is a promising electrolyte material for AEMFCs.

Due to the free volume effect brought by the four-arm star shaped structure, the qPTTP-7 membrane is advantageous in term of hydroxide ion conductivity and stability, which gave rise to higher fuel cell power density and durability than some of the recently reported AEMs (Fig. 8) such as QPEPTpi-35 (1200 mW cm^{-2}, 20 h),[44] QABNP (1160 mW cm^{-2}, 30 h),[1] PDTP-10 (732 mW cm^{-2}, 14 h),[40] and PPTDF-QA-2.5 (778 mW cm^{-2}, 60 h).[11] Therefore, it can be concluded that qPTTP-7 AEM has a good potential for application in fuel cells.

4 Conclusions

In summary, we have employed a straightforward methodology to fabricate 4-arm star shaped poly(aryl piperidine) AEMs. The optimized qPTTP-7 membrane demonstrates a high OH^- conductivity exceeding 140 mS cm^{-1} at 80 °C, coupled with favorable characteristics in terms of water uptake and swelling ratio. Meanwhile, it exhibits commendable mechanical properties and resistance to degradation, remaining structurally intact even after prolonged exposure to a highly alkaline environment (1 M NaOH) at 80 °C for 3000 hours. The application of this membrane in AEMFCs yields a peak power density of 1.37 W cm^{-2} in H_2–O_2 fuel cells. And AEMFCs utilizing qPTTP-7 demonstrate good performance over the course of 150 h. This work provides a novel and effective strategy for enhancing both OH^- conductivity and alkali stability of AEMs employed in fuel cells.

Author contributions

Long Han: conceptualization, investigation, methodology, formal analysis, visualization, writing original draft. Shoutao Gong: investigation, data curation, formal analysis, visualization. Xinli Zhang: investigation, methodology. Min Yang: investigation. Xiaoming Yan: project administration, methodology. Gaohong He: project administration, funding acquisition. Fengxiang Zhang: conceptualization, writing – review & editing, project administration, funding acquisition, supervision.

Conflicts of interest

There are no conflicts to declare.

Acknowledgements

This work was supported by the Fund of National Natural Science Foundation of China (Grant no. 22075037), the Creative Group Fund of National Natural Science Foundation of China (Grant no. 22021005), and the Fundamental Research Fund for the Central Universities of China (Grant no. DUT19ZD214).

References

1 W. T. Gao, X. L. Gao, W. W. Gou, J. J. Wang, Z. H. Cai, Q. G. Zhang, A. M. Zhu and Q. L. Liu, *J. Membr. Sci.*, 2022, **655**, 120578.
2 E. N. Hu, C. X. Lin, F. H. Liu, X. Q. Wang, Q. G. Zhang, A. M. Zhu and Q. L. Liu, *J. Membr. Sci.*, 2018, **550**, 254–265.
3 L. Liu, W. Ma, J. Zhang, Z. Liu, D. Chu, R. Shao, S. Chen, X. Chu and N. Li, *J. Membr. Sci.*, 2023, **678**, 121663.
4 Y. Ahn and D. Kim, *J. Ind. Eng. Chem.*, 2019, **71**, 361–368.
5 J. H. Chen, X. B. Yue, Y. S. L. Choo, Z. Yu, X. H. Wang, X. L. Gao, W. T. Gao, Q. G. Zhang, A. M. Zhu and Q. L. Liu, *J. Power Sources*, 2023, **570**, 233014.
6 J. Liu, X. Yan, L. Gao, L. Hu, X. Wu, Y. Dai, X. Ruan and G. He, *J. Membr. Sci.*, 2019, **581**, 82–92.
7 L. Bai, L. Ma, L. Li, A. Zhang, X. Yan, F. Zhang and G. He, *ACS Appl. Energy Mater.*, 2021, **4**, 6957–6967.
8 H. Chen, K. T. Bang, Y. Tian, C. Hu, R. Tao, Y. Yuan, R. Wang, D. M. Shin, M. Shao, Y. M. Lee and Y. Kim, *Angew. Chem., Int. Ed.*, 2023, **62**, e202307690.
9 D. R. Dekel, S. Willdorf, U. Ash, M. Amar, S. Pusara, S. Dhara, S. Srebnik and C. E. Diesendruck, *J. Power Sources*, 2018, **375**, 351–360.
10 Y. J. Liu, W. T. Gao, A. M. Zhu, Q. G. Zhang and Q. L. Liu, *J. Membr. Sci.*, 2023, **687**, 122045.
11 X. Li, B. Zhang, J. Guo, Y. Chen, L. Dai, J. Zheng, S. Li and S. Zhang, *J. Mater. Chem. A*, 2023, **11**, 10738–10747.
12 J. S. Olsson, T. H. Pham and P. Jannasch, *Adv. Funct. Mater.*, 2017, **28**, 1702758.
13 J. Pan, C. Chen, Y. Li, L. Wang, L. Tan, G. Li, X. Tang, L. Xiao, J. Lu and L. Zhuang, *Energy Environ. Sci.*, 2014, **7**, 354–360.
14 S. Proch, M. Stenström, L. Eriksson, J. Andersson, G. Sjöblom, A. Jansson and J. Westlinder, *Int. J. Hydrogen Energy*, 2020, **45**, 1313–1324.
15 X. Zhang, J. Guo, X. Chu, C. Fang, Y. Huang, L. Liu and N. Li, *J. Membr. Sci.*, 2022, **659**, 120820.
16 J. Zhao, N. Li, S. Wang, Y. Wang, Y. Lei, J. Wu, Y. Zhang, J. Yu, F. Wang, Z. Sui, J. Gao and Z. Wang, *Next Energy*, 2023, **1**, 100075.
17 Z. Y. Zhu, W. W. Gou, J. H. Chen, Q. G. Zhang, A. M. Zhu and Q. L. Liu, *J. Membr. Sci.*, 2021, **636**, 119569.
18 Q. Liu, W. Ma, L. Tian, J. Li, L. Yang, F. Wang, Z. Wang, J. Li, Z. Wang and H. Zhu, *J. Power Sources*, 2022, **551**, 232105.
19 J. Yan and M. A. Hickner, *Macromolecules*, 2010, **43**, 2349–2356.
20 D. Yao, T. Wei, L. Shang, H. Na and C. Zhao, *RSC Adv.*, 2019, **9**, 7975–7983.
21 M. M. Hossain, J. Hou, L. Wu, Q. Ge, X. Liang, A. N. Mondal and T. Xu, *J. Membr. Sci.*, 2018, **550**, 101–109.
22 J. Pan, L. Zhu, J. Han and M. A. Hickner, *Chem. Mater.*, 2015, **27**, 6689–6698.
23 S. Willdorf-Cohen, A. N. Mondal, D. R. Dekel and C. E. Diesendruck, *J. Mater. Chem. A*, 2018, **6**, 22234–22239.
24 X. Wu, N. Chen, C. Hu, H. A. Klok, Y. M. Lee and X. Hu, *Adv. Mater.*, 2023, **35**, 202210432.

25 W. H. Lee, Y. S. Kim and C. Bae, *ACS Macro Lett.*, 2015, **4**, 814–818.
26 C. Hu, J. H. Park, H. M. Kim, H. H. Wang, J. Y. Bae, N. Y. Kang, N. Chen and Y. M. Lee, *J. Membr. Sci.*, 2022, **647**, 120341.
27 G. Xu, J. Pan, X. Zou, Z. Jin, J. Zhang, P. Fang, Q. Zhang, Z. Sun and F. Yan, *Adv. Funct. Mater.*, 2023, **33**, 2302364.
28 L. Ma, M. Hussain, L. Li, N. A. Qaisrani, L. Bai, Y. Jia, X. Yan, F. Zhang and G. He, *J. Membr. Sci.*, 2021, **636**, 119529.
29 J. Zhang, K. Zhang, X. Liang, W. Yu, X. Ge, M. A. Shehzad, Z. Ge, Z. Yang, L. Wu and T. Xu, *J. Mater. Chem. A*, 2021, **9**, 327–337.
30 M.-a. Kakimoto, S. J. Grunzinger and T. Hayakawa, *Polym. J.*, 2010, **42**, 697–705.
31 Z. Yang, Y. Liu, R. Guo, J. Hou, L. Wu and T. Xu, *Chem. Commun.*, 2016, **52**, 2788–2791.
32 X. Wang, C. Lin, Y. Gao and R. G. H. Lammertink, *J. Membr. Sci.*, 2021, **635**, 110525.
33 X. Qiao, X. Wang, S. Liu, Y. Shen and N. Li, *J. Membr. Sci.*, 2021, **630**, 119325.
34 Q. Yang, Y. Y. Cai, Z. Y. Zhu, L. X. Sun, Y. S. L. Choo, Q. G. Zhang, A. M. Zhu and Q. L. Liu, *ACS Appl. Mater. Interfaces*, 2020, **12**, 24806–24816.
35 Z. Yu, W. T. Gao, Y. J. Liu, Q. G. Zhang, A. M. Zhu and Q. L. Liu, *J. Colloid Interface Sci.*, 2023, **651**, 404–414.
36 Q. Liu, S. Zhang, L. Tian, J. Li, W. Ma, F. Wang, Z. Wang, J. Li and H. Zhu, *J. Power Sources*, 2023, **564**, 232822.
37 L. Tian, J. Li, Q. Liu, W. Ma, F. Wang, H. Zhu and Z. Wang, *ACS Appl. Mater. Interfaces*, 2022, **14**, 39343–39353.
38 C. Wei, W. Yu, Y. Zhang, F. Zhang, M. Li, X. Shen, K. Zhang, X. Ge, L. Wu and T. Xu, *J. Power Sources*, 2023, **553**, 232247.
39 L. Liu, Y. Deng, W. Zhang, J. Zhang, W. Ma, L. Li, X. Zhang and N. Li, *J. Membr. Sci.*, 2023, **672**, 121441.
40 X. Wang, X. Qiao, S. Liu, L. Liu and N. Li, *J. Membr. Sci.*, 2022, **653**, 120558.
41 K. Min, J. E. Chae, Y. Lee, H.-J. Kim and T.-H. Kim, *J. Membr. Sci.*, 2022, **653**, 120487.
42 L. Ma, L. Li, M. Yuan, L. Bai, A. Zhang, X. Yan, G. He and F. Zhang, *ACS Sustain. Chem. Eng.*, 2022, **10**, 5748–5757.
43 W. Song, X. Liang, H. Zhang, X. Liu, X. Zhang, L. Wu, X. Ge and T. Xu, *J. Mater. Chem. A*, 2022, **10**, 21503–21511.
44 J. Liu, L. Gao, X. Ruan, W. Zheng, X. Yan and G. He, *Chem. Eng. J.*, 2023, **471**, 144574.